Available online at www.sciencedirect.com

jmr&t Journal of Materials Research and Technology

journal homepage: www.elsevier.com/locate/jmrt

Original Article

Radiation shielding and mechanical properties of mullite-zirconia composites fabricated from investment-casting shell waste

Celal Avcıoğlu [a,b,*], Maged F. Bekheet [a], R. Artır [b]

[a] Technische Universität Berlin, Faculty III Process Sciences, Institute of Material Science and Technology, Fachgebiet Keramische Werkstoffe / Chair of Advanced Ceramic Materials, Straße des 17. Juni 135, 10623, Berlin, Germany
[b] Marmara University, Faculty of Engineering, Department of Metallurgical and Materials Engineering, 34722, Istanbul, Turkey

ARTICLE INFO

Article history:
Received 19 January 2023
Accepted 20 April 2023
Available online 25 April 2023

Keywords:
Mechanical properties
Investment casting shell waste
Ceramic recycling
Mullite zirconia ceramic composite
Gamma radiation shielding

ABSTRACT

Low-cost zirconia-toughened mullite composites were prepared from investment casting shell waste and alumina. The influence of sintering temperature on the composites' properties, including crystalline phase composition, microstructure, degrees of densification, mechanical properties, and radiation shielding characteristics, was investigated. The results show that the higher the sintering temperature, the higher the degree of densification is, improving the mechanical and radiation shielding properties of prepared composites. The mullite-zirconia composite sintered at 1600 °C presents a good mechanical strength, with flexural and compressive strength values of 190 and 308 MPa, respectively. These values are comparable to or even better than mullite ceramics prepared from other waste materials. Furthermore, the composites' gamma-ray and neutron attenuation characteristics suggest that they can be promising as radiation shields.

1. Introduction

The growing global economy and fierce industrial competition are leading to severe environmental deterioration and the unsustainable exploitation of natural resources. To achieve a greener and more sustainable economy, shifting toward sustainable production patterns with low ecological footprints is essential. Investment casting, a lost wax casting, is one of the most widely used manufacturing processes for fabricating complex-shaped metal components. In this process, molten metal is poured into a disposable ceramic mold and then solidified. Afterward, ceramic shell molds are broken off, and the casted metals are collected [1]. Accordingly, the investment casting industry generates millions of tons of refractory investment casting shell waste annually [2].

Ceramic shell molds are typically made of valuable refractory materials, including silica, mullite, and zircon. Nevertheless, due to the stringent requirements of the casting process, waste shell molds cannot be recycled or reused. Therefore, waste ceramic shell molds are usually disposed to landfills. Hence, developing an economically feasible

* Corresponding author.
E-mail address: celal.avcioglu@ceramics.tu-berlin.de (C. Avcıoğlu).
https://doi.org/10.1016/j.jmrt.2023.04.190

recycling process that brings value to this waste is highly desirable.

Mullite is an important phase of the SiO_2–Al_2O_3 binary system owing to its high melting point (1840 °C), low thermal expansion coefficient (6·10–6/°C), low density (3.20 g/cm^3), high chemical stability, and good thermal shock, creep and corrosion resistance [3]. Therefore, mullite ceramics are commonly used as refractories, catalysts, catalytic supports, membranes, and radiation shields [4–6].

Solid-state reaction synthesis using industrial-grade regents is the most common route to obtain mullite ceramics [7]. Nevertheless, recent years have witnessed a surge of interest in producing mullite ceramics from industrial wastes to reduce raw materials cost. Indeed, various silica or alumina-rich waste materials, such as aluminum sludge, aluminum dross, metakaolin, coal fly ash, rice husk, waste glasses, and slate waste, have been utilized to fabricate mullite ceramics [4,8].

However, the mechanical properties of mullite ceramics fabricated from industrial wastes were generally lower than that synthesized from reagent-grade raw materials [8,9]. Although mullite ceramics might suffer from low bending strength and fracture toughness at room temperature, they could be commonly reinforced with second-phase enhancers such as carbon fiber, Al_2O_3, ZrO_2, B_4C, Al_2O_3, SiC, TiC, WC, etc. [10–15]. Another approach to improve the mechanical properties of mullite ceramics is self-strengthening through microstructure tailoring, in which columnar mullite grains with interlocking structures are attained during synthesis. Previous studies demonstrated that various sintering aids, such as CeO_2 and Cr_2O_3, La_2O_3, MgO, and Y_2O_3, can promote the formation of columnar mullite grains [16,17]. Among these additives, MgO was also reported to play a positive role in the dissociation of zircon and stabilization of tetragonal zirconia [16,18–20].

This investigation aimed to assess the feasibility of investment casting shell waste as a raw material in producing high-density mullite-zirconia ceramics. The prepared specimens containing a determined amount of alumina and investment casting shell waste were sintered at 1450–1600 °C. The influence of additives and sintering temperature on the various properties of as-prepared mullite-zirconia composites, including crystalline phase composition, microstructure, porosity, density, linear shrinkage, radiation shielding, and mechanical properties, was investigated in detail. To the best of our knowledge, this is the first study evaluating the radiation shielding characterizations of zirconia-mullite ceramics.

2. Characterization of CW and experimental procedures

Large chunks of CW were obtained from a local plant in Turkey's Marmara province and broken in a jaw crusher to approximately 1 mm in size. Then, the crushed CW was ground via a mortar grinder (Pulverisette 2, Fritsch, Germany) for 5 min to obtain a particle size lesser than 63 μm. The images of the CW before and after grinding and particle size distributions of the ground powder are presented in Fig. 1a. As shown in Fig. 1c, ground CW powder has an angular morphology, and its grain size distribution is consistent with particle size measurement results. SEM/EDS elemental mapping images show that CW powder mainly consists of Si, Al, Zr, and O, but small amounts of Ti and Fe are also present. The chemical compositions of the CW as determined by XRF analysis (Rigaku RSX, Japan) are listed in Table 1. The results of XRD are in agreement with those of XRF. The main phases in CW include silica, mullite, and zircon (Fig. 1b).

Mullite-zirconia composites were synthesized as follows. According to the above chemical compositions (Table 1) and to obtain 3:2 mullite ($3Al_2O_3 \cdot 2SiO_2$) in the final composite, CW powder and Al_2O_3 (Merck, 45 μm mean particle size and ≥99.9% purity) were proportioned in mass ratios of 100:82. Thereby, the following reactions may occur during heat treatment:

$$2SiO_2 + 3Al_2O_3 = Al_6Si_2O_{13} \quad (1)$$

$$2ZrSiO_4 + 3Al_2O_3 = 2ZrO_2 + Al_6Si_2O_{13} \quad (2)$$

Three other compositions were also formulated by adding 1 wt % MgO, TiO_2, or V_2O_5 sintering additives to the powder mixture. The powder mixtures prepared were mixed in distilled water via a planetary ball mill at a speed of 400 rpm for 2 h using a zirconia jar and high-purity alumina grinding media, then dried overnight at 80 °C and crushed in an agate mortar with a pestle. The obtained powder mixtures were mixed with both 1 wt% polyvinyl alcohol and stearic acid, which serve as a binder and internal lubricant, respectively. First, PVA was dissolved in distilled water at 70 °C and stirred for 20 min before being added to the powder mixture and continued the stirring process for 2 h, then dried overnight at 70 °C and crushed in an agate mortar with pestle. The same procedure was applied for stearic acid, but acetone was used as a solvent. Rectangular (50 mm × 20 mm x 8 mm), disc-shaped (12 mm × 5 mm), and cubic (12 mm × 12 mm x 12 mm) green bodies obtained by uni-axial pressing by applying a pressure of 200 Mpa, followed by debinding at 500 °C for 2 h with the heating rate of 2 °C min^{-1} in an electrical furnace. Then, the sintering process was conducted in air at 1450 °C, 1500 °C, 1550 °C, and 1600 °C. The heating and cooling rate was 5 °C min^{-1}, and the dwelling period at the maximum temperature was 4 h. The sample codes, batch compositions, and their sintering temperatures are given in Table 2.

Phase compositions of samples analyzed by X-ray powder technique with a D8 Advance X-ray diffractometer (Bruker, Germany) using CuKα radiation (λ = 1.5406 Å). The microstructure of samples was analyzed with scanning electron microscopy (Quanta Feg 250, FEI, USA). Linear shrinkage of samples was determined by measuring the diameter of green and sintered bodies. Density and open porosity were measured by the Archimedes method. The compression and three-point bending tests were performed in a RetroLine testing machine (Zwick/Roell, Ulm, Germany) using cube (10 mm × 10 mm x 10 mm) and bar (20 mm × 8 mm x 8 mm) shaped sintered bodies respectively, and a cross head speed of 0.5 mm/min applied. EpiXS and PhyX/PSD programs were used to theoretically explore the radiation shielding ability of manufactured ceramics. More information on the computational methods can be found in the literature [21–23].

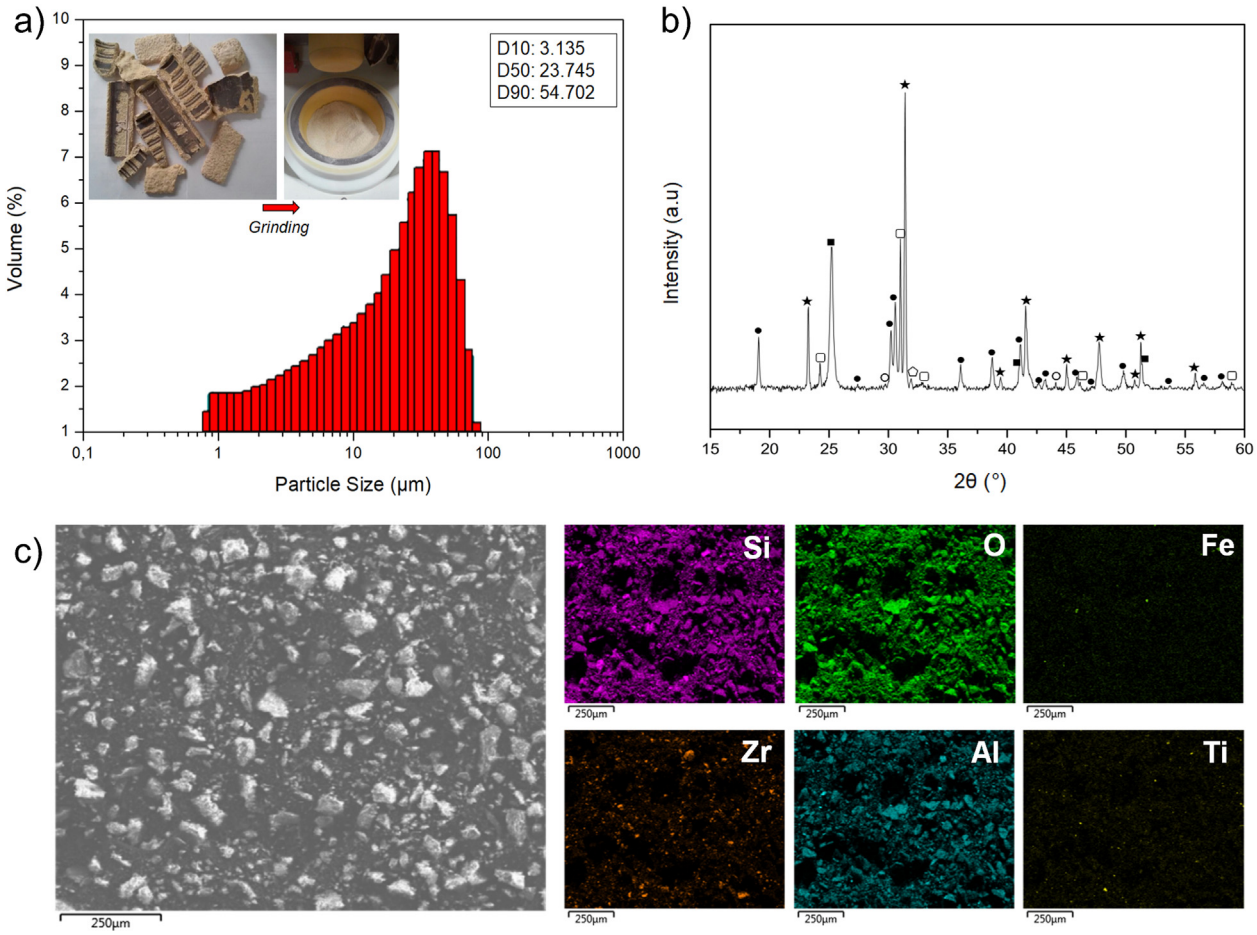

Fig. 1 – (a) The particle size distributions of the ground CW powder. Inset: photographs of the CW before and after grinding and the D10, D50, and D90 values. (b) XRD pattern of CW powder (★ = zircon, ● = mullite, ■ = cristobalite, ▢ = quartz, and ⬠ = TiO_2). (c) SEM and EDS mapping images of the ground CW powder.

3. Results and discussion

The XRD patterns of the samples heated at 1450 °C are shown in Fig. 2. It can be seen that the CW1450 sample, sintered without adding any sintering additives, is composed of mullite and zircon ($ZrSiO_4$) crystalline phases, evidencing the mullite formation reactions among the silica and alumina in the starting materials have been completed after the heat treatment at 1450 °C.

The dissociation of zircon into ZrO_2 and SiO_2 usually starts at 1673 ± 10 °C [24]. Nonetheless, impurities may promote zircon dissociation at lower temperatures [24–26]. However, no zircon dissociation is observed neither in CW1450 sintered without additives nor in CW1450-T and CW1450–V samples containing TiO_2 and V_2O_5 additives, respectively. Contrarily, the XRD patterns of the CW1450-M sample containing 1 wt% of MgO additive show characteristic XRD peaks belonging to mullite, zircon, tetragonal ZrO_2, and monoclinic ZrO_2 phases. These results indicate that the MgO additive promotes zircon ($ZrSiO_4$) dissociation.

It's worth noting that zircon dissociates into silica and tetragonal zirconia at elevated temperatures. Indeed, the tetragonal phase is the stable phase of zirconia above 1170 °C, and it might be transformed into the monoclinic phase during the cooling from 1170 °C [27,28]. Nevertheless, the presence of the tetragonal phase in CW1450-M might be attributed to the stabilization effect of the additive MgO [29]. As the sintering temperature is increased from 1450 °C to 1500 °C, the zircon content significantly decreases (Fig. 3). By further increasing

Table 1 – Elemental composition (wt-%) of CW powder determined from XRF analysis.

Al	Si	Ca	Ti	Fe	Sr	Zr	Nb	Na	P	K	O
14.78	24.79	0.14	1.85	0.45	0.05	12.33	0.02	0.04	0.03	0.16	45.77

Table 2 – Sample codes, batch compositions, and sintering temperatures of the ceramic bodies.

Sample	Sintering Temperature (°C)	Composition (wt.%)				
		W	Al_2O_3	MgO	TiO_2	V_2O_5
CW1450	1450	54.9	45.1	–	–	–
CW1450-M	1450	54.4	44.6	1	–	–
CW1450-T	1450	54.4	44.6	–	1	–
CW1450–V	1450	54.4	44.6	–	–	1
CW1500-M	1500	54.4	44.6	1	–	–
CW1550-M	1550	54.4	44.6	1	–	–
CW1600-M	1600	54.4	44.6	1	–	–

the sintering temperature to 1550 °C, the XRD peaks corresponding to the zircon phase completely disappeared. The zircon decomposition reaction is reversible, and zirconia and silica phases recombine to form zircon during cooling. However, no zircon peaks are detectable in the XRD patterns of the CW1550-M and CW1600-M samples. This observation can be attributed to the alumina additive, which presumably consumes the silica to yield mullite. It is also worth pointing out that CW1450-M contains monoclinic and tetragonal zirconia phases, whereas the samples sintered at higher temperatures contain no tetragonal zirconia. This is likely related to the growth of zirconia grains with increasing sintering temperature. Indeed, the earlier investigations on zirconia ceramics' tetragonal to monoclinic phase transformation have confirmed that increasing the grain size favors this transformation. In contrast, sub-micron grain size is often required to obtain tetragonal phase zirconia [28].

The linear shrinkage, bulk density, and apparent porosity of the sintered composites are shown in Fig. 4. A noticeable linear shrinkage of 15.2% is observed for the CW1500-M. The linear shrinkage increases with sintering temperature, reaching 19.4% for the sample sintered at 1600 °C. This trend is consistent with bulk density and apparent porosity results. When the sintering temperature increases from 1500 to 1550 °C, the apparent porosity decreases from ~5.4 to ~2.3%, while the bulk density adversely increases from 2.62 to 2.66 g cm^{-3}, as shown in Table 3. Increasing the sintering temperature to 1600 °C results in an enhanced bulk density of 2.87 g cm^{-3}.

The SEM micrographs of the fractured and polished surfaces of samples are represented in Fig. 5. As shown in Fig. 5a, the CW1500-M sample sintered at 1500 °C comprises consolidated angular grains. Increasing the sintering temperature from 1500 °C to 1550 °C leads to the formation of elongated mullite crystals with curved edges and corners (Fig. 5c). On the other hand, the CW1600-M composite shows similar microstructural development as CW1550-M, but the grain size of mullites is larger due to the Ostwald ripening (Fig. 5e). Notably, the formation of elongated mullite crystals is usually accompanied by the consumption of the surrounding matrix. As a result, mullite crystals were generally encapsulated by closed porosities (Fig. 5e and 5f-inset).

It is now well established that the elongated morphology is a characteristic of mullite crystals grown in a vitreous phase. Furthermore, the curved edges and corners of mullite grains indicate their formation occurred in the liquid phase. The formation of elongated mullite grains can be attributed to the presence of impurity TiO_2 and Fe_2O_3 phases in the investment-casting shell waste or to the MgO additive, as they all reported to form transient liquid phases that promote the growth of mullite grains in elongated morphologies [20,30,31].

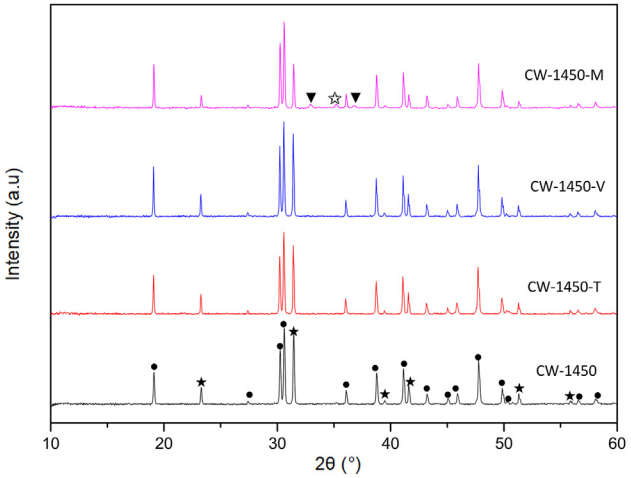

Fig. 2 – XRD patterns of the CW1450, CW1450-T, CW1450–V, and CW1450-M, samples. (★ = zircon, ● = mullite, ▼ = *m*-ZrO_2, and ☆ = t-ZrO_2).

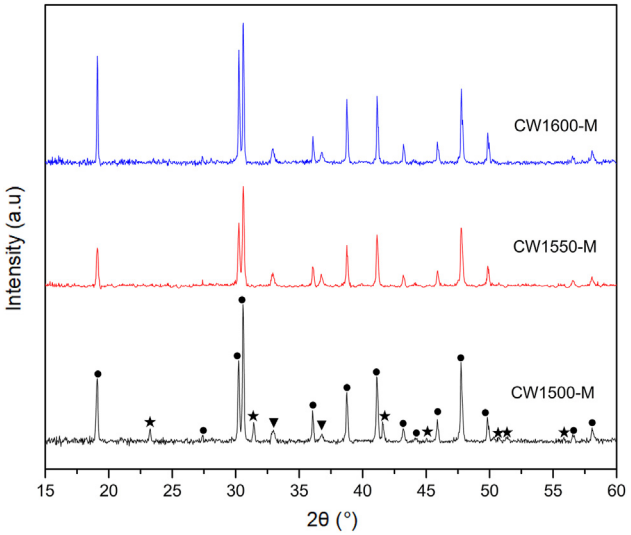

Fig. 3 – XRD patterns of the CW1500-M, CW1550-M, and CW1600-M samples. (★ = zircon, ● = mullite, and ▼ = *m*-ZrO_2).

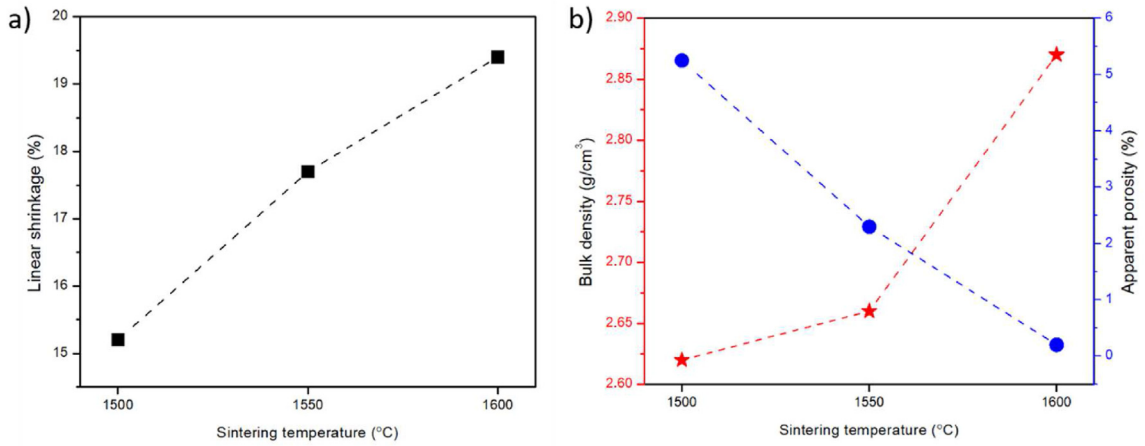

Fig. 4 – (a) Linear shrinkage, (b) bulk density, and (c) apparent porosity values of the CW1500-M, CW1550-M, and CW1600-M samples.

The micrograph of the samples with polished surfaces reveals that they consist of irregular zirconia grains with bright contrast distributed in a mullite matrix exhibiting a grey contrast (Fig. 5b). The size of zirconia grains is in the submicron range, approximately up to 5 μm.

The compression and flexural strength values of the as-prepared composites and the relevant research on the mullite ceramics reported in the literature are summarized in Table 4. As the compression and flexural strength were enhanced by increasing the sintering temperature, a correlation between mechanical properties and density can be inferred. Besides, such enhancement in the mechanical properties might also be attributed to the formation of elongated-shaped mullite grains with interlocking structures and the toughening effect of zirconia via crack deflection and microcracking mechanisms [32–35]. The highest compression and flexural strengths are determined for the CW1600-M composite, with approximately 308 and 190 MPa, respectively. These values are comparable to or even better than most mullite ceramics and mullite-containing composites fabricated from recycled raw materials. Indeed, the flexural strength of developed ceramic composites delivered from investment casting shell waste is considerably higher than its counterparts. This is probably due to the formation of interlocking elongated mullite structures, which are more beneficial to flexural strength than compression strength. However, the mechanical properties are slightly lower than some mullite-zirconia ceramics prepared from fine and pure starting powders due to the closed porosities and impurities in the composites. It is worth stressing that green bodies here were prepared by uniaxial pressing. Besides, the raw materials were coarse; hence, zirconia in these composites was monoclinic. If isostatic or hot pressing is applied and zirconia can be stabilized in the tetragonal phase, then larger strength values could definitely be obtained.

Table 3 – Measured density and the weight fraction of constituent compounds of the CW1500-M, CW1550-M, and CW1600-M samples.

Sample names	Density (g/cm^3)	The weight fraction of constituent compounds (%)		
		$Al_6Si_2O_7$	ZrO_2	$ZrSiO_4$
CW1500-M	2.62	93	4	3
CW1550-M	2.66	93	7	–
CW1600-M	2.87	93	7	–

The attenuation of gamma rays occurs through the interaction of the gamma radiation with matter's electrons via multiple absorption and scattering processes. The total cross-section is an important parameter of radiation shielding materials, and it is a measure of the probability of photons interacting with the shielding material. As seen in Fig. 6a, all samples exhibit nearly identical cross-section variations due to their similar chemical compositions. The total cross-section drastically decreases in the low-energy region as photon energy increases to approximately 80 keV. Then, the degree of decrease rate reduces in the photon energy range of 80–6000 keV region. Nevertheless, the cross-section values slowly rise as photon energy further increases. Such drastic changes in the total cross-section values originate from the processes involved in gamma ray-matter interactions in different photon energy regions.

Fig. 6b–d illustrates the dominant photon-matter interaction mechanisms for varying energy regions. It can be seen that the photoelectric effect, incoherent scattering (Compton scattering), and pair production are the main processes involved in gamma-ray-matter interactions for all samples. Photoelectric absorption proceeds through the interaction of gamma-ray with an inner shell electron of the matter, which results in the total transfer of gamma-ray energy to the exciting electron. Therefore, elements with higher atomic numbers provide better gamma shielding through the photoelectric absorption mechanism. For the fabricated composites, the photoelectric absorption mechanism dominates the gamma attenuation process in the low-energy region up to 80 keV. As seen in Table 3, CW1600-M and CW1550-M contain slightly larger zirconium than CW1500-M. Zirconium

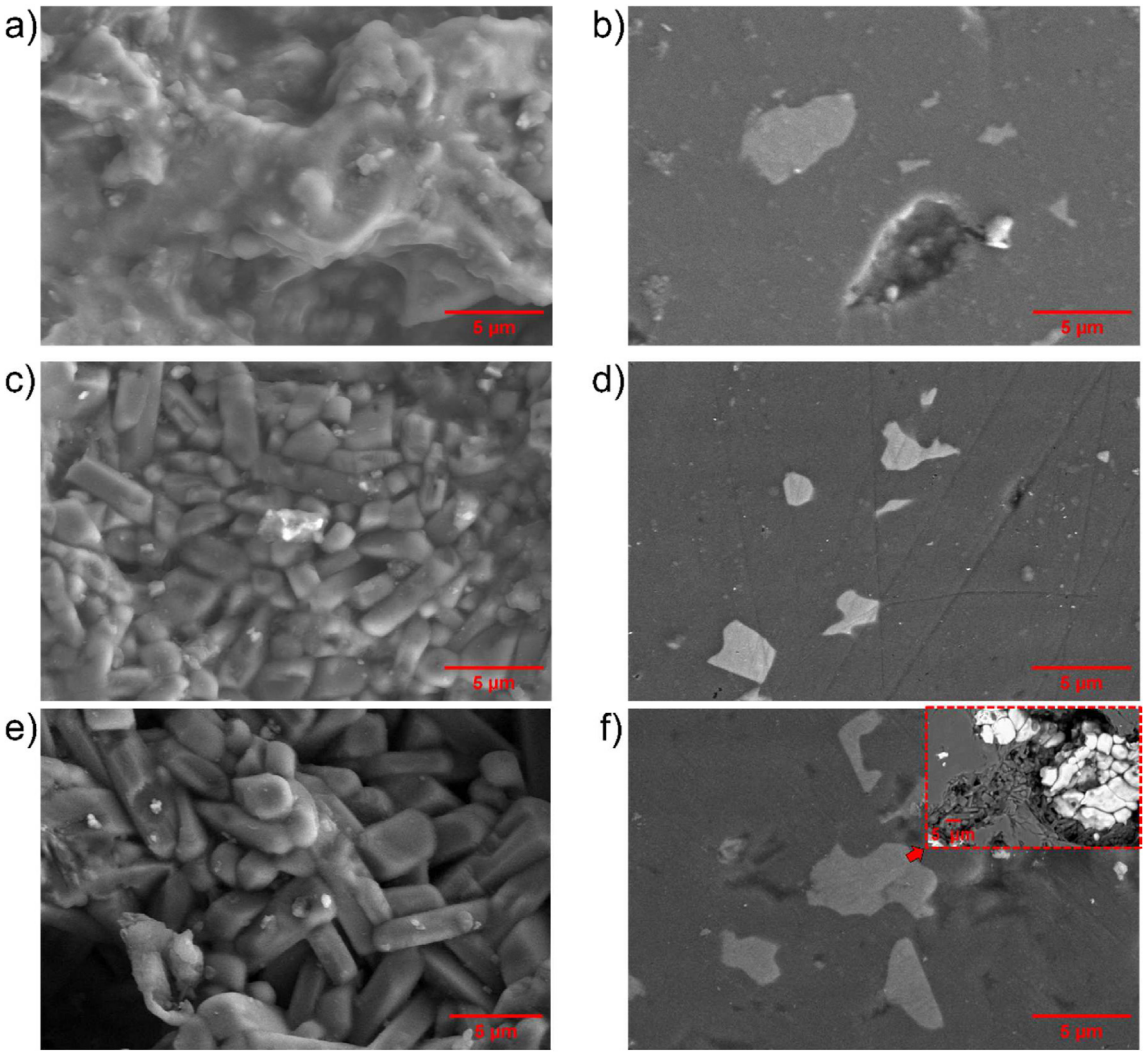

Fig. 5 – SEM images of the (a, c, d) fractured and (b, d, f) polished surfaces of the (a, b) CW1500-M, (c, d) CW1550-M, and (e, f) CW1600-M samples.

possesses a higher atomic number than aluminum and silicon. Therefore, its abundance in CW1600-M and CW1550-M provides better gamma attenuation relative to CW1500-M (inset of Fig. 6a). From 80 to 6000 keV, incoherent scattering becomes dominant. When a photon interacts with a charged particle, most frequently an electron, it scatters incoherently and loses energy. This phenomenon is also called the Compton effect and involves the partial transfer of the photons' energy to the recoiling electron [52]. Fig. 6d indicates that the CW1600-M sample can attenuate gamma rays up to approximately 20,000 keV via the incoherent scattering mechanism. When the photon's energy exceeds 20,000 keV, a high-energy pair production phenomenon becomes a dominant attenuation mechanism. In this phenomenon, high-energy photons interact with the nucleus, forming subatomic particle pairs such as an electron and a positron [52].

Linear attenuation coefficient (μ) is a constant that describes the fraction of attenuated gamma rays per unit thickness of matter. The linear attenuation coefficient can be expressed by Beer-Lambert law as fallow;

$$I = I_0 e^{-\mu x} \quad (3)$$

μ (cm^{-1}) is the material's linear attenuation, x (cm) is the thickness of the material, I_0 is the incident beam intensity, and I is the intensity after attenuation [53,54]. Linear attenuation coefficient (μ) can be further converted into a material constant called the mass attenuation coefficient (μ_ρ; cm^2/g) by simply dividing it by the density of the shielding material. The linear and mass attenuation coefficients of the fabricated composites in the energy region between 1 keV and 1000 MeV are presented in Fig. 7. The results show that increasing sintering temperature led to an increase in the samples' linear attenuation coefficients. Indeed, the CW1600-M sample demonstrates a relatively higher linear attenuation coefficient than both CW1500-M and CW1550-M samples in the whole photon energy region. The probability of an interaction between the radiation and the absorber's atoms decreases with increasing porosity [55]. Therefore, it is reasonable that a low-density absorber provides less attenuation than a high-density absorber. Nevertheless, all samples exhibit similar

Table 4 – The mechanical properties of mullite/zirconia composites prepared in this work compared to different mullites reported in the literature.

Final product	Raw materials	Sintering temperature (°C)	Sintering method	Compression strength (MPa)	Flexural strength (MPa)	Ref.
Mullite/zirconia composite	Investment casting shell waste and alumina	1500	Reaction sintering	164	134	This work
Mullite/zirconia composite	Investment casting shell waste and alumina	1550	Reaction sintering	232	170	This work
Mullite/zirconia composite	Investment casting shell waste and alumina	1600	Reaction sintering	308	190	This work
Mullite	bauxite and industrial waste fly ash	1600	Reaction sintering	–	186	[36]
Mullite	alumina and coal fly ash	1500	Reaction sintering	–	169	[37]
V-doped Mullite	high-aluminum fly ash, bauxite and vanadium oxide	1500	Reaction sintering	–	108	[38]
mullite/corundum composite	industrial waste fly ash, bauxite	1500	Reaction sintering	–	115	[39]
Mullite/zirconia composite	Aluminum nitrate nonahydrate, TEOS, and monoclinic zirconia	1700	Sol-gel preparation technique followed by reaction sintering	–	83.30	[40]
Mullite/cordierite composite	Fumed silica, alumina, and magnesia	1400	Reaction sintering	180	–	[41]
Mullite	High-aluminum fly ash	1600	Alkali and acid treatment followed by reaction sintering	169	–	[42]
Y-doped Mullite/zirconia composite	Alumina, silica-gel, monoclinic zirconia, yttrium oxide	1250	Spark plasma sintering	~335		[43]
Ce-doped Mullite	Alumina, silica, and cerium oxide	1650	Reaction sintering	308		[35]
Mullite/zirconia composite	Aluminum sulfate, sodium silicate, and zirconium chloride	1500	co-precipitation method followed by spark plasma sintering	–	289	[44]
Mullite/zirconia composite	Mullite and yttria-stabilized zirconia	1500	Reaction sintering	–	190	[45]
Mullite/zirconia composite	Electrofused Mullite/zirconia composite and zircon	1600	Slip casting	–	~176	[46]
Mullite/zirconia composite	Zircon flour and sillimanite beach sand	1600	Reaction sintering	–	245.9	[47]
Mullite/zirconia/alumina	Zircon and alumina	1650	Reaction sintering	–	~173	[48]
/zircon composite	Zircon and mullite	1600	Slip casting	–	~210	[49]
Ti-doped Mullite/zirconia composite	Alumina, silica, zirconia, and titanium oxide	1500	Hot pressing	–	674.05	[50]
Mullite/alumina/zirconia/silicon carbide	Alumina, silica, yttria-stabilized zirconia, and silicon carbide	1530	Hot pressing	–	970	[51]

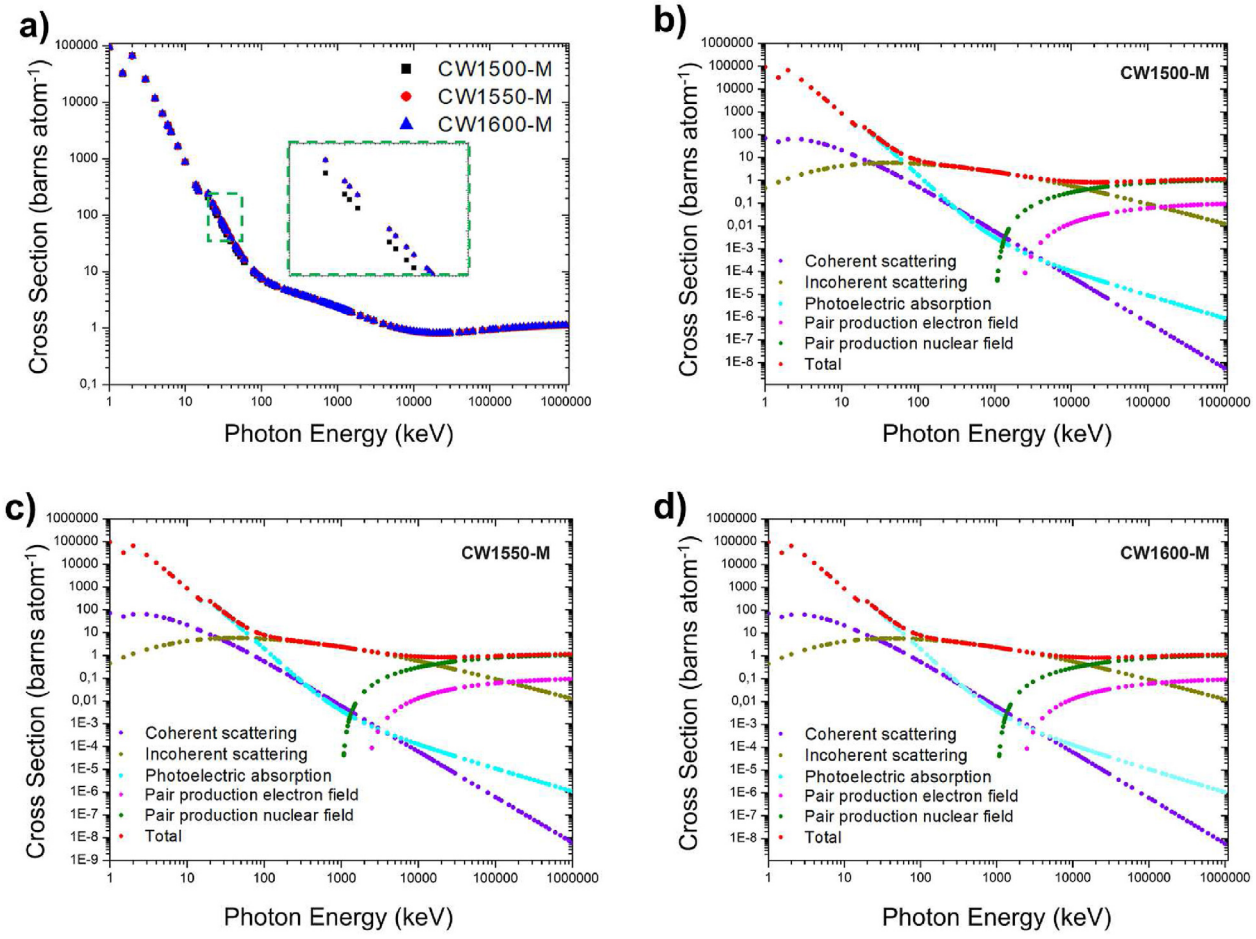

Fig. 6 – (a) The relative variations of the total cross section for the CW1500-M, CW1550-M, and CW1600-M samples vs. photon energy. The relationship between the photon energy and cross-section of (b) CW1500-M, (c) CW1550-M, and (d) CW1600-M in the energy range from 1 to 10^6 keV.

mass attenuation coefficient variations due to their similar chemical compositions, as seen in Fig. 7b.

The mean free path (MFP), the average distance a photon can travel before interacting with the shielding material, can be determined from the linear attenuation coefficient using equation (4) [21].

$$MFP = 1/\mu \tag{4}$$

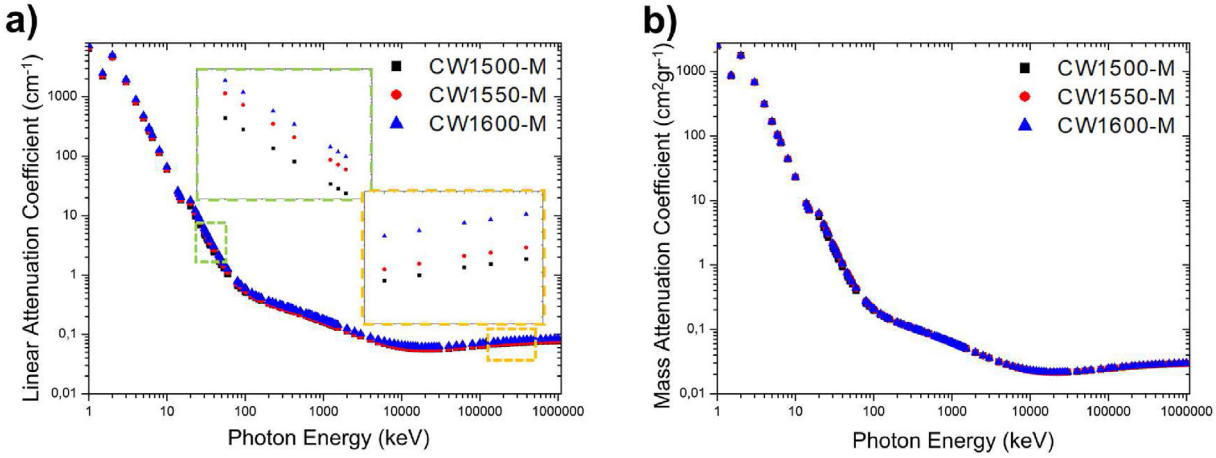

Fig. 7 – The relative variations of (a) linear attenuation coefficient and (b) mass attenuation coefficient for the CW1500-M, CW1550-M, and CW1600-M samples vs. photon energy. The insets in (a) show amplified graphs of emphasized regions.

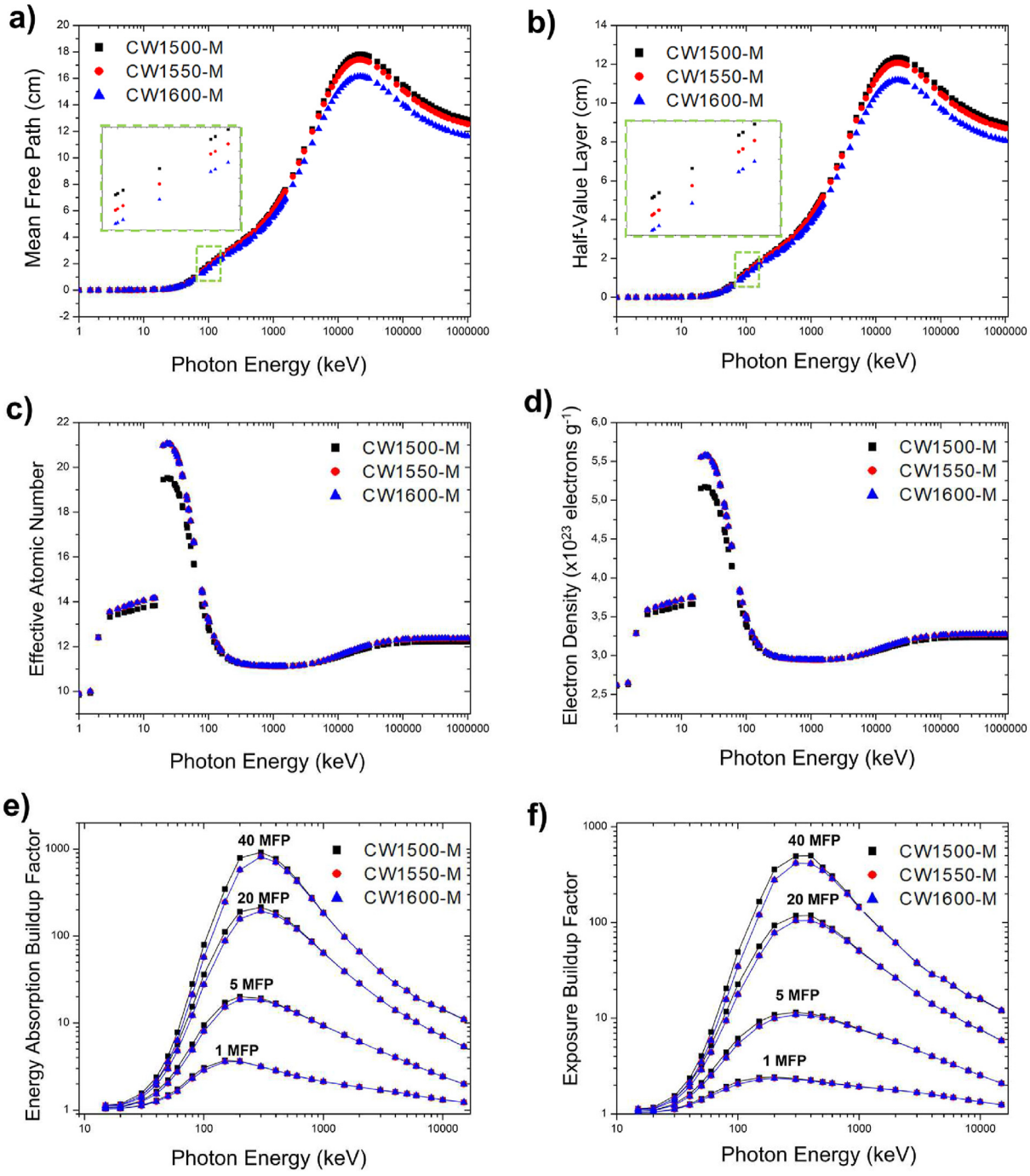

Fig. 8 – The relative variations of (a) the mean free path (MFP), (b) half-value layer (HVL), (c) effective atomic number (Zeff), (d) electron density (Neff), (e) energy absorption buildup factor (EABF), and (f) exposure buildup factor (EBF) for the CW1500-M, CW1550-M, and CW1600-M samples vs. photon energy.

The MFP variation results of fabricated ceramics are presented in Fig. 8a. It has been found that MFP values for all ceramic samples remain almost zero, up to roughly 30 keV photon energy. This means that photons with low energy photons cannot be penetrated deeply into the fabricated ceramics. Although the MFP values steadily rise with increasing photon energy from 30 keV to 100 keV, they remain lower than 2 cm for all ceramic composites. Nonetheless, a sharper increase is observed beyond the photon energy of 100 keV. Meanwhile, the difference between the MFP values of the ceramic samples is enlarged. The maximum MFP values for all composites were noticed against photons with ~20 MeV energy.

The half-value layer (HVL) is another important parameter for radiation shielding materials, that is, the required material thickness to reduce the radiation intensity by 50%. HVL can be expressed using the following equation [21].

$$HVL = \ln(2)/\mu \quad (5)$$

As shown in Fig. 8b, HVL values demonstrate a similar trend as the MFP values for all ceramic composites. The

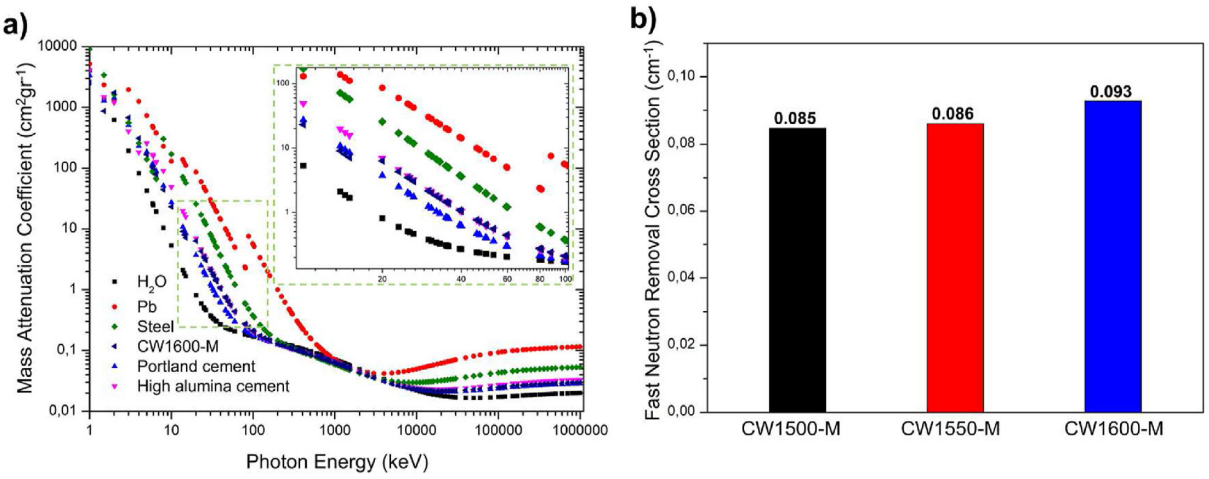

Fig. 9 – (a) Comparison of the mass attenuation coefficient variations of commonly used radiation shielding materials with CW1600-M (b) The fast neutron removal cross-sections of CW1500-M, CW1550-M, and CW1600-M samples computed using the PhysX software.

highest HVL thickness is observed at a photon energy of ~20 MeV for all samples. The maximum HVL values of CW1500-M, CW1550-M, and CW1600-M are 12.35, 12.07, and 11.19 cm, respectively. The CW1600-M sample possesses the lowest MFP and HVL values in the whole photon energy range due to its higher density and zirconium content.

The effective atomic number (Z_{eff}) and electron density (N_{eff}) variations of fabricated ceramic composites are also investigated. The results indicate that Z_{eff} and N_{eff} reach their maximum values at around 23 keV photon energy due to a K-shell absorption edge (Fig. 8c–d). Following the maxima, a gradual decrease in both Z_{eff} and N_{eff} is observed with increasing photon energy. Because CW1550-M and CW1600-M have the same chemical composition, their Z_{eff} and N_{eff} variations are expected to be similar. On the other hand, due to its lower zirconium content, the CW1500-M sample shows slightly lower Z_{eff} and N_{eff} values in the whole photon energy range.

The variations of the energy absorption buildup factor (EABF) and exposure buildup factor (EBF) at various penetration depths are depicted in Fig. 8e and f, respectively. These figures demonstrate that EABF and EBF values initially rise with increasing photon energy. They both reach their peak value at 300 keV and then decline. The observed trend is due to changing dominant photon-matter interaction mechanisms in different energy regions [56,57]. Lower EABF and EBF values indicate a greater radiation shielding performance. Figs. 6 and 7 show that the photoelectric effect is dominating in the low-energy region. Because the photoelectric effect is a highly efficient gamma attenuation mechanism, EABF and EBF values remain fairly low until the photon energy of approximately 100 keV for all ceramic composites.

Nonetheless, multiple scattering events occur at higher photon energies when Compton scattering dominates attenuation, where EABF and EBF values reach their peaks. With a further increase in photon energy, the pair production mechanism becomes dominant in the attenuation process, which results in a reducing trend in the EABF and EBF values [56,57]. Moreover, there is a dramatic increase in the EABF and EBF values when the penetration depth increases from 1 MFP to 40 MFP. This can be ascribed to increased scattering events within the ceramics. It is also worth mentioning that there is a direct correlation between total cross-sections and the EABF and EBF values.

To better assess the radiation shielding performance of the fabricated ceramic composites, the mass attenuation coefficient and fast neutron removal cross-section results of the CW1600-M sample are compared with commonly used radiation shielding materials. As seen in Fig. 9a, the CW1600-M sample exhibits greater mass attenuation coefficient values than that of the Portland cement and water for the entire photon energy region. Meanwhile, it demonstrates comparable mass attenuation coefficient results to high alumina cement for the whole energy range.

Fig. 9b displays the fast neutron removal cross-sections of samples. It can be seen that the CW1600-M sample provides a relatively higher fast neutron removal cross-section ($\Sigma R = 0.093\ cm^{-1}$) than other samples due to its higher density. Furthermore, the CW1600-M sample also outperforms two extensively used neutron shielding materials, graphite ($\Sigma R = 0.077\ cm^{-1}$) and paraffin ($\Sigma R = 0.0773\ cm^{-1}$), whereas its fast neutron removal cross-section is comparable to that of concrete ($\Sigma R = 0.094\ cm^{-1}$) [58,59].

4. Conclusion

This investigation aimed to assess the feasibility of investment casting shell waste as a raw material in producing high-performance mullite-zirconia ceramics. The following conclusions can be drawn from the present study.

(1) XRD analysis revealed that investment casting shell waste consists of mullite, silica, and zircon, providing the required raw materials to produce mullite-zirconia ceramic composites.

(2) The silica in the investment casting shell waste reacted entirely with alumina to yield mullite at sintering temperatures higher than 1450 °C.
(3) Since zirconia phases can be formed in the ceramic composites through the decomposition of the zircon phase in the investment casting shell waste, three sintering additives, including TiO_2, V_2O_5, and MgO, were tested to promote the zircon dissociation. Only the MgO additive could effectively complete the zircon dissociation, but at a high sintering temperature of at least 1550 °C when 1 wt% MgO was used.
(4) The mechanical properties of the composites were enhanced with increasing sintering temperature from 1500 °C to 1600 °C. Indeed, the sample sintered at 1600 °C for 4 h exhibited higher bulk density, flexural strength, and compressive strength than other samples. The bulk density, flexural strength, and compressive strength of CW-1600 M were 2.87 g cm^{-3}, 190, and 308 MPa, respectively. These values are relatively better than most mullite ceramics fabricated from other waste materials. The relatively good mechanical properties of the composites were attributed to the formation of elongated-shaped mullite grains with interlocking structures and the toughening effect of zirconia via the crack deflection and microcracking mechanisms.
(5) Theoretical investigations demonstrated that density strongly influences the samples' gamma- and neutron-shielding properties. Indeed, the sample sintered at 1600 °C displayed greater shielding parameters than others due to its higher density. Its gamma- and neutron-shielding properties are comparable to commonly used radiation shields.

Accordingly, this study demonstrates a plausible way to utilize investment casting shell waste.

CRediT author statement

C.Avcıoğlu: Conceptualization, Investigation, Data Curation, Visualization, Writing - Original Draft, Writing - Review & Editing. M.F. Bekheet: Writing - Review & Editing. R. Artır: Supervision, Resources, Writing- Review & Editing. All authors ratified the submitted and revised versions.

Declaration of competing interest

The authors declare that they have no known competing financial interests or personal relationships that could have appeared to influence the work reported in this paper.

Acknowledgment

We acknowledge the support from the German Research Foundation and the Open Access Publication Fund of TU Berlin.

REFERENCES

[1] Reference module in materials science and materials engineering. Elsevier; 2016.
[2] Xiang R, Li Y, Li S, Xue S, He Z, Ouyang S, Nana X. The potential usage of waste foundry sand from investment casting in refractory industry. J Clean Prod 2019;211:1322–7. https://doi.org/10.1016/j.jclepro.2018.11.280.
[3] Lecomte-Nana GL, Hammas A. Mullite: structure and properties. In: Pomeroy M, editor. Encyclopedia of materials: technical ceramics and glasses. Oxford: Elsevier; 2021. p. 59–75.
[4] Abdullayev A, Bekheet MF, Hanaor DAH, Gurlo A. Materials and applications for low-cost ceramic membranes. Membranes 2019;9(9):105. https://doi.org/10.3390/membranes9090105.
[5] Abdullayev A, Klimm D, Kamutzki F, Gurlo A, Bekheet MF. AlF3-assisted flux growth of mullite whiskers and their application in fabrication of porous mullite-alumina monoliths. Open Ceramics 2021;7:100145. https://doi.org/10.1016/j.oceram.2021.100145.
[6] Abdullayev A, Avcioglu C, Fey T, Hilger A, Osenberg M, Manke I, et al. Fabrication and characterization of porous mullite ceramics derived from fluoride-assisted Metakaolin-Al(OH)3 annealing for filtration applications. Open Ceramics 2022;9:100240. https://doi.org/10.1016/j.oceram.2022.100240.
[7] Abdullayev A, Zemke F, Gurlo A, Bekheet MF. Low-temperature fluoride-assisted synthesis of mullite whiskers. RSC Adv 2020;10(52):31180–6. https://doi.org/10.1039/D0RA05997H.
[8] Choo Salleh M, Kok Matori. A Review on synthesis of mullite ceramics from industrial wastes. Recycling 2019;4(3):39. https://doi.org/10.3390/recycling4030039.
[9] Mizuno M. Microstructure, microchemistry, and flexural strength of mullite ceramics. J Am Ceram Soc 1991;74(12):3017–22. https://doi.org/10.1111/j.1151-2916.1991.tb04295.x.
[10] Ghasali E, Saeidabadi EK, alizadeh M, Fazili A, Rajaei H, Jam A, et al. Preparation of mullite/B4C composites: a comparative study on the effect of heating methods. Ceram Int 2018;44(15):18743–51. https://doi.org/10.1016/j.ceramint.2018.07.104.
[11] Ertugrul O, Dalmis R, Akpinar S, Kusoglu IM, Celik E. Influence of zircon particle size on conventional and microwave assisted reaction sintering of in-situ mullite–zirconia composites. Ceram Int 2016;42(9):11104–17. https://doi.org/10.1016/j.ceramint.2016.04.016.
[12] Hirata Y, Itoh S, Shimonosono T, Sameshima S. Theoretical and experimental analyses of Young's modulus and thermal expansion coefficient of the alumina-mullite system. Ceram Int 2016;42(15):17067–73. https://doi.org/10.1016/j.ceramint.2016.07.216.
[13] Rajaei H, Farvizi M, Mobasherpour I, Zakeri M. Effect of spark plasma sintering temperature on microstructure and mechanical properties of mullite - WC composites. Int J Refract Metals Hard Mater 2018;70:197–201. https://doi.org/10.1016/j.ijrmhm.2017.10.012.
[14] Ghahremani D, Ebadzadeh T, Maghsodipour A. Densification, microstructure and mechanical properties of Mullite–TiC composites prepared by spark plasma sintering. Ceram Int 2015;41(2):1957–62. https://doi.org/10.1016/j.ceramint.2014.07.146.
[15] Jing Y, Deng X, Li J, Bai C, Jiang W. Fabrication and properties of SiC/mullite composite porous ceramics. Ceram Int 2014;40(1):1329–34. https://doi.org/10.1016/j.ceramint.2013.07.013.

[16] Maitra S, Pal S, Nath S, Pandey A, Lodha R. Role of MgO and Cr2O3 additives on the properties of zirconia–mullite composites. Ceram Int 2002;28(7):819–26. https://doi.org/10.1016/S0272-8842(02)00048-2.
[17] Sarraf F, Abbatinali E, Gorjan L, Sebastian T, Colombo P, Churakov SV, et al. Effect of MgO sintering additive on mullite structures manufactured by fused deposition modeling (FDM) technology. J Eur Ceram Soc 2021;41(13):6677–86. https://doi.org/10.1016/j.jeurceramsoc.2021.06.012.
[18] El-Tawil SZ, El-Barawy KA, Francis AA. Cubic zirconia from zircon sand by firing with CaO/MgO mixture. J. Ceram. Soc. Japan 1999;107(1243):193–8. https://doi.org/10.2109/jcersj.107.193.
[19] Quadling A, Vandeperre L, Parkes M, Lee WE. Second phase-induced degradation of fused MgO partially stabilized zirconia aggregates. J Am Ceram Soc 2015;98(4):1364–71. https://doi.org/10.1111/jace.13458.
[20] Prusty S, Mishra DK, Mohapatra BK, Singh SK. Effect of MgO in the microstructure formation of zirconia mullite composites from sillimanite and zircon. Ceram Int 2012;38(3):2363–8. https://doi.org/10.1016/j.ceramint.2011.10.089.
[21] Şakar E, Özpolat ÖF, Alım B, Sayyed MI, Kurudirek M. Phy-X/PSD: development of a user friendly online software for calculation of parameters relevant to radiation shielding and dosimetry. Radiat Phys Chem 2020;166:108496. https://doi.org/10.1016/j.radphyschem.2019.108496.
[22] Şakar E, Özpolat Ö, Alım B, Alsaif NA, Rammah YS. Evaluation of γ-rays and neutron shielding parameters of high dense bismo-boro-tellurite glasses: comparative study. Radiat Phys Chem 2022;196:110149. https://doi.org/10.1016/j.radphyschem.2022.110149.
[23] Hila FC, Asuncion-Astronomo A, Dingle CAM, Jecong JFM, Javier-Hila AMV, Gili MBZ, et al. EpiXS: a Windows-based program for photon attenuation, dosimetry and shielding based on EPICS2017 (ENDF/B-VIII) and EPDL97 (ENDF/B-VI.8). Radiat Phys Chem 2021;182:109331. https://doi.org/10.1016/j.radphyschem.2020.109331.
[24] Kaiser A, Lobert M, Telle R. Thermal stability of zircon (ZrSiO4). J Eur Ceram Soc 2008;28(11):2199–211. https://doi.org/10.1016/j.jeurceramsoc.2007.12.040.
[25] Kenny GG, Pasek MA. The response of zircon to the extreme pressures and temperatures of a lightning strike. Sci Rep 2021;11(1):1560. https://doi.org/10.1038/s41598-021-81043-8.
[26] Burger W, Kiefer G. Alumina, zirconia and their composite ceramics with properties tailored for medical applications. J. Compos. Sci. 2021;5(11):306. https://doi.org/10.3390/jcs5110306.
[27] Pavlik RS, Holland HJ, Payzant EA. Thermal decomposition of zircon refractories. J Am Ceram Soc 2001;84(12):2930–6. https://doi.org/10.1111/j.1151-2916.2001.tb01117.x.
[28] Köck E-M, Kogler M, Götsch T, Schlicker L, Bekheet MF, Doran A, et al. Surface chemistry of pure tetragonal ZrO2 and gas-phase dependence of the tetragonal-to-monoclinic ZrO2 transformation. Dalton Trans 2017;46(14):4554–70. https://doi.org/10.1039/C6DT04847A.
[29] Porter DL, Heuer AH. Microstructural development in MgO-partially stabilized zirconia (Mg-PSZ). J Am Ceram Soc 1979;62(5–6):298–305. https://doi.org/10.1111/j.1151-2916.1979.tb09484.x.
[30] Suhasinee Behera P, Bhattacharyya S. Sintering and microstructural study of mullite prepared from kaolinite and reactive alumina: effect of MgO and TiO 2. Int J Appl Ceram Technol 2021;18(1):81–90. https://doi.org/10.1111/ijac.13637.
[31] Huang CS, Liu JC, Guo AR, Yang L, Song Di. Effects of SiO_2 and Fe_2O_3 on morphological of mullite. High-Performance Ceramics VI 2010;434–435:64–5. https://doi.org/10.4028/www.scientific.net/KEM.434-435.64.
[32] Glymond D, Vick MJ, Giuliani F, Vandeperre LJ. High-temperature fracture toughness of mullite with monoclinic zirconia. J Am Ceram Soc 2017;100(4):1570–7. https://doi.org/10.1111/jace.14637.
[33] Mochales C, Maerten A, Rack A, Cloetens P, Mueller WD, Zaslansky P, et al. Monoclinic phase transformations of zirconia-based dental prostheses, induced by clinically practised surface manipulations. Acta Biomater 2011;7(7):2994–3002. https://doi.org/10.1016/j.actbio.2011.04.007.
[34] Rühle M, Evans AG, McMeeking RM, Charalambides PG, Hutchinson JW. Microcrack toughening in alumina/zirconia. Acta Metall 1987;35(11):2701–10. https://doi.org/10.1016/0001-6160(87)90269-0.
[35] Zhu X, Chen L, Zhao F, Gao J, Li K, Liu X, et al. A novel strategy to fabricate high-strength mullite by the reaction sintering method using Al3+/Ce4+-doped SiO2. Ceram Int 2021;47(9):13129–38. https://doi.org/10.1016/j.ceramint.2021.01.177.
[36] Dong Y, Feng X, Feng X, Ding Y, Liu X, Meng G. Preparation of low-cost mullite ceramics from natural bauxite and industrial waste fly ash. J Alloys Compd 2008;460(1–2):599–606. https://doi.org/10.1016/j.jallcom.2007.06.023.
[37] Jung JS, Park HC, Stevens R. Mullite ceramics derived from coal fly ash. J Mater Sci Lett 2001;20(12):1089–91. https://doi.org/10.1023/A:1010934728570.
[38] Li J-H, Ma H-W, Huang W-H. Effect of V2O5 on the properties of mullite ceramics synthesized from high-aluminum fly ash and bauxite. J Hazard Mater 2009;166(2–3):1535–9. https://doi.org/10.1016/j.jhazmat.2008.11.059.
[39] Cao J, Dong X, Li L, Dong Y, Hampshire S. Recycling of waste fly ash for production of porous mullite ceramic membrane supports with increased porosity. J Eur Ceram Soc 2014;34(13):3181–94. https://doi.org/10.1016/j.jeurceramsoc.2014.04.011.
[40] Abdallah AI, Sayed M, Awaad M, Yousif AHE, Naga SM. Characterization of in-situ zirconia/mullite composites prepared by sol-gel technique. Journal of Asian Ceramic Societies 2021:1. https://doi.org/10.1080/21870764.2021.1929738. –7.
[41] Khattab RM, EL-Rafei AM, Zawrah MF. In situ formation of sintered cordierite–mullite nano–micro composites by utilizing of waste silica fume. Mater Res Bull 2012;47(9):2662–7. https://doi.org/10.1016/j.materresbull.2012.04.036.
[42] Lin B, Li S, Hou X, Li H. Preparation of high performance mullite ceramics from high-aluminum fly ash by an effective method. J Alloys Compd 2015;623:359–61. https://doi.org/10.1016/j.jallcom.2014.11.023.
[43] Sedmale G, Sperberga I, Zilinska N, Steins I. Spark plasma sintering (SPS) to the mullite –zirconia ceramics development. ms 2015;21(1):96–9. https://doi.org/10.5755/j01.ms.21.1.5501.
[44] School of High Temperature Materials and Magnesium Resource Engineering, University of Science and Technology Liaoning, Anshan 114051, China, State Key Laboratory of New Ceramics and Fine Processing, School of Materials Science and Engineering, Tsinghua University, Beijing 100084, China. Zirconia-mullite obtained from Co-precipitated zirconia-mullite composite powders by SPS. J Ceram Sci Technol 2016;7(4):417–422.
[45] Hemra K, Aungkavattana P. Effect of zirconia content on mechanical and thermal properties of mullite–zirconia composite. Adv Appl Ceram 2014;113(6):323–7. https://doi.org/10.1179/1743676114Y.0000000164.

[46] Rendtorff NM, Garrido LB, Aglietti EF. Zirconia toughening of mullite–zirconia–zircon composites obtained by direct sintering. Ceram Int 2010;36(2):781–8. https://doi.org/10.1016/j.ceramint.2009.11.010.
[47] Kumar P, Nath M, Ghosh A, Tripathi HS. Synthesis and characterization of mullite–zirconia composites by reaction sintering of zircon flour and sillimanite beach sand. Bull Mater Sci 2015;38(6):1539–44. https://doi.org/10.1007/s12034-015-0890-3.
[48] Besisa DHA, Ewais EMM. Investigation of mechanical strength of the functionally graded zirconia-mullite/alumina ceramics tailored for high temperature applications. Mater Res Express 2019;6(7):75516. https://doi.org/10.1088/2053-1591/ab177e.
[49] Rendtorff NM, Garrido LB, Aglietti EF. Mechanical and fracture properties of zircon–mullite composites obtained by direct sintering. Ceram Int 2009;35(7):2907–13. https://doi.org/10.1016/j.ceramint.2009.03.040.
[50] Yu H, Chen Y, Guo X, Luo L, Li J, Li W, et al. Study on mechanical properties of hot pressing sintered mullite-ZrO2 composites with finite element method. Ceram Int 2018;44(7):7509–14. https://doi.org/10.1016/j.ceramint.2018.01.146.
[51] Chen X, Luo L, Liu L, Li J, Yu H, Li W, et al. Microstructure and mechanical properties of hot-pressed Al2O3–mullite–ZrO2–SiC composites. Mater Sci Eng, A 2019;740–741. https://doi.org/10.1016/j.msea.2018.10.118. 390–7.
[52] Podgoršak EB. Interactions of photons with matter. In: Radiation physics for medical physicists. Berlin, Heidelberg: Springer; 2009. p. 277–375.
[53] Avcıoğlu S, Buldu M, Kaya F, Üstündağ CB, Kam E, Menceloğlu YZ, et al. Processing and properties of boron carbide (B4C) reinforced LDPE composites for radiation shielding. Ceram Int 2020;46(1):343–52. https://doi.org/10.1016/j.ceramint.2019.08.268.
[54] Avcıoğlu S, Buldu M, Kaya F, Kaya C. Chapter 20 - synthesis of nuclear-grade nano-sized boron carbide powders and its application in LDPE matrix composites for neutron shielding. In: Low I-M, Dong Y, editors. Composite materials manufacturing, properties and applications. Elsevier; uuuu-uuuu, p. 543–579.
[55] Chen S, Bourham M, Rabiei A. Applications of open-cell and closed-cell metal foams for radiation shielding. Procedia Materials Science 2014;4:293–8. https://doi.org/10.1016/j.mspro.2014.07.560.
[56] Sayyed MI, AlZaatreh MY, Dong MG, Zaid M, Matori KA, Tekin HO. A comprehensive study of the energy absorption and exposure buildup factors of different bricks for gamma-rays shielding. Results Phys 2017;7:2528–33. https://doi.org/10.1016/j.rinp.2017.07.028.
[57] Avcioğlu S. LDPE matrix composites reinforced with dysprosium-boron containing compounds for radiation shielding applications. J Alloys Compd 2022;927:166900. https://doi.org/10.1016/j.jallcom.2022.166900.
[58] Ilik E, Kavaz E, Kilic G, Issa SA, Zakaly HM, Tekin HO. A closer-look on Copper(II) oxide reinforced Calcium-Borate glasses: fabrication and multiple experimental assessment on optical, structural, physical, and experimental neutron/gamma shielding properties. Ceram Int 2022;48(5):6780–91. https://doi.org/10.1016/j.ceramint.2021.11.229.
[59] Sallam OI, Madbouly AM, Moussa NL, Abdel-Galil A. Impact of radiation on CoO-doped borate glass: lead-free radiation shielding. Appl Phys A 2022;128(1):1–16. https://doi.org/10.1007/s00339-021-05190-5.